High Interfacial Charge Storage Capability of Carbonaceous Cathodes for Mg Batteries

Lu Wang,[†] Bo Jiang,[†] Per Erik Vullum,[‡,§] Ann Mari Svensson,[†] Andreas Erbe,[†] Sverre M. Selbach,[†] Huailiang Xu,[∥] and Fride Vullum-Bruer*[†]

[†]Department of Materials Science and Engineering, Norwegian University of Science and Technology, NO-7491 Trondheim, Norway

[‡]SINTEF Materials and Chemistry, 7491 Trondheim, Norway

[§]Department of Physics, Norwegian University of Science and Technology, 7491 Trondheim, Norway

[∥]The Sixth Element Materials Technology Co., Ltd., 213000 Changzhou, China

*E-mail: fride.vullum-bruer@ntnu.no

ABSTRACT: A rechargeable Mg battery where the capacity mainly originates from reversible reactions occurring at the electrode/electrolyte interface efficiently avoids the challenge of sluggish Mg intercalation encountered in conventional Mg batteries. The interfacial reactions in a cell based on microwave exfoliated graphite oxide (MEGO) as the cathode, and all phenyl complex (APC) as electrolyte, are by quantitative kinetics analysis identified as a combination of diffusion-controlled reactions involving ether solvents (*esol*s) and capacitive processes. During magnesiation, *esol*s in APC electrolytes can significantly affect the electrochemical reactions and charge transfer resistances at the electrode/electrolyte interface, and thus govern the charge storage properties of the MEGO cathode. In APC-tetrahydrofuran (THF) electrolyte, MEGO exhibits a reversible capacity of ~220 mAh g^{-1} at 10 mA g^{-1}, while a reversible capacity of ~750 mAh g^{-1} at 10 mA g^{-1} was obtained in APC-1,2-dimethoxyethane (DME) electrolyte. The high capacity improvement not only points to the important role of the *esol*s in the APC electrolytes, but also presents a Mg battery with high interfacial charge storage capability as a very promising and viable competitor to the conventional intercalation-based batteries.

KEYWORDS: Mg battery, microwave exfoliated graphite oxide, diffusion-controlled reactions, ether solvents, capacitive processes

Mg batteries have been considered an attractive alternative to Li-based energy storage due to the abundant and inexpensive resources, as well as their chemical stability.[1,2] Mg does not suffer from dendrite formation during electrochemical deposition/dissolution, which eliminates a significant safety issue that has hindered the application of Li-ion batteries utilizing a Li metal anode in large scale energy storage.[3,4] Compared with Li, Mg has significantly higher theoretical volumetric capacity (3833 mAh cm^{-3}), which is nearly twice that of Li (2061 mAh cm^{-3}). This indicates the potential for Mg batteries to reach high volumetric energy densities.[5,6] For Mg batteries to be commercially viable, it is important to place significant focus on the development of electrolytes, since the electrolyte properties determine the working potential range and the class of available cathode materials.[7,8] So far, several promising Mg electrolytes have been developed, *e.g.* Mg-Al chloride complex (MACC) electrolyte,[9] $Mg(PF_6)_2$-based electrolytes,[10] $Mg(TFSI)_2$-based electrolytes,[11] $Mg(BH_4)_2$-based electrolytes,[12] and APC electrolyte, which is the well-known Mg organohaloaluminate electrolyte.[13-15] The studies with APC electrolyte done by Aurbach *et al.* revealed that this chemical system (see Part 1, Supporting Information for more details) is far more complex than electrolytes used for Li-ion batteries, according to characterizations by NMR and Raman.[15] Moreover, Muldoon *et al.* demonstrated that the oxidative stability of the APC electrolyte is in excess of 3 V vs Mg when Pt is used as working electrode (WE).[16] However, the chloride components of the Mg organohaloaluminates cause severe corrosion of metals, such as the stainless steel casing of the coin cells, and traditional metal current collectors, *e.g.* Cu foil, Al foil or Ni foil. This corrosion limits the operation window to below 2.2 V vs Mg in a coin cell battery configuration.[17-19] With this concern in mind, use of carbonaceous materials (*e.g.* graphite foil (Gif), glassy carbon or carbon cloth) as current collectors is suggested due to their natural

chemical inertness towards Mg electrolytes.[5,7,20-24] Gif shows a similar voltage window to Pt in accordance with our previous study.[25]

Although the electrolyte plays an important role in the battery performance, it is also vital to have a good cathode material which can provide the desired capacity. It has however, been proven quite challenging to find highly reversible intercalation materials which are comparable to those used in commercial Li-ion batteries. While the ionic radii of Mg^{2+} and Li^+ are similar, the 2+ charge on Mg causes strong coulombic interactions with the intercalation host due to its higher charge density.[1,2] Such interactions make the ion diffusion sluggish, resulting in a low Mg intercalation level and a large difference between the charge and discharge potentials. Thus, the choice of cathodes for Mg batteries is limited because of the difficulty associated with the intercalation of Mg^{2+} cations into various inorganic compounds. Some classes of materials which have been proposed as potential Mg^{2+} intercalation cathodes include the Chevrel-phase compounds (based on Mo_6S_8),[26,27] layer structured MoO_3,[28-30] MoS_2 nanosheets,[31,32] and thiospinel Ti_2S_4.[33] However, most of these provide relatively modest specific capacities (~100 mAh g^{-1}) due to the sluggish diffusion of Mg^{2+} cations in the host lattice. In addition to the issue of poor Mg^{2+} diffusion, the high charge density of Mg^{2+} may also cause slower solvation (in the electrolyte)-desolvation (at the cathode/electrolyte interface) processes compared with the Li-ion system.[34,35] Arthur *et al.*[36] indicated that the Mg complex has a low degree of dissociation due to the strong interaction between the Mg cations and coordinated species. This may lead to only partial desolvation of Mg complexes at the electrode/electrolyte interface. It is well-known that the interfacial properties significantly impact the cell performance, since the interfacial redox reactions depend on ion diffusion across this interface.[35] Hence, the surface properties of the cathode in a given electrolyte (*e.g.* APC electrolyte) are crucial as they directly determine the degree of dissociation of the Mg

complex. This issue has been studied by several research groups.[2,34,37] Aurbach *et al.* pointed out that the Mg complex can be readily desolvated in APC electrolyte, benefiting the Mg intercalation into Mo_6S_8.[2] The high degree of desolvation is a key factor for the performance of Mo_6S_8 as Mg battery cathode.[34,37] However, on the surface of most inorganic compounds, the degree of desolvation of the Mg complex is much lower, greatly restricting the selection of electrode materials available for Mg batteries.[2]

Basically, the current situation for both cathodes and electrolytes are in need of significant improvements for further development of Mg batteries. One prospective strategy to circumvent the Mg^{2+} intercalation issue is the utilization of a battery system where the capacity depends on the electrochemical behaviour at the electrode/electrolyte interface rather than on Mg^{2+} intercalation. As Dunn *et al.* reported in their studies, electrochemical reactions that are limited by the surface, and not by solid-state diffusion, could enable electrodes with high rate capability.[38] The surface-limited reactions can be capacitive processes (which serve as the mechanism in a typical supercapacitor) and/or faradaic reactions occurring at the electrode/electrolyte interface. It has also been proven that both the capacitive contribution and the total stored charge could be dramatically enhanced by using nano-sized materials as electrodes for Li-ion batteries.[39,40] Shen *et al.*[41] reported a substantial capacitive contribution in Na-ion batteries with SnS/graphene as the anode. Capacitive effects have also been investigated for Mg batteries.[21,23,42] However, none of them show stable cycling performances close to the order of what is found in supercapacitors, which has been realized in Mg batteries based on sponge-like Mn_3O_4 as cathode and APC solution as electrolyte, according to our previous work.[25] With contributions from interfacial charge storage, including both the capacitive effect and the contribution from the solvent-related interfacial reactions, Mn_3O_4 cathodes exhibited ~100% coulombic efficiencies at various current

rates and negligible capacity decay after one thousand cycles. In light of this work, utilization and development of the interfacial charge storage mechanism could be an effective strategy to enhance the electrochemical performance of Mg batteries.

Here, it is proposed to utilize MEGO, which was obtained through the exfoliation of graphite oxide (GiO) under the treatment of microwave irradiation according to Ruoff's work,[43] as a cathode material in APC electrolytes. The synthesized MEGO, with the combination of its conductive networks, large surface area and substantial surface defects, displayed high rate capabilities (225 mAh g^{-1} at 10 mA g^{-1} and 125 mAh g^{-1} at 1 A g^{-1}), and stable cycling performance in APC-THF electrolyte. This excellent cell performance can be attributed to the fast kinetics of the capacitive behaviour as well as high reversibility of the ether solvent (*esol*)-related interfacial reactions. In addition to the ring-structured THF solvent, the chain-structured DME, G2 (diglyme) and G4 (tetraglyme) *esol*s have been investigated in order to evaluate the effect of varying *esol*s on the cell performance. Based on the quantitative kinetic analysis and the measured electrochemical performances of the MEGO cathode along with density functional theory (DFT) calculations, it was demonstrated that the electrochemical performance of the MEGO cathode in APC electrolytes is determined by the structure of the *esol*s. Strikingly, in APC-DME electrolyte, the MEGO cathode exhibits, to the best of our knowledge, the highest reversible capacity measured (~750 mAh g^{-1} at 10 mA g^{-1}) for any Mg battery electrode, cathode or anode. The materials also exhibited excellent cycling stability (94% retention after 500 cycles at 500 mA g^{-1}). These promising results pose an interesting development for Mg batteries, which may be able to circumvent the issues caused by the slow diffusion kinetics of Mg cations in the bulk.

Results/Discussion
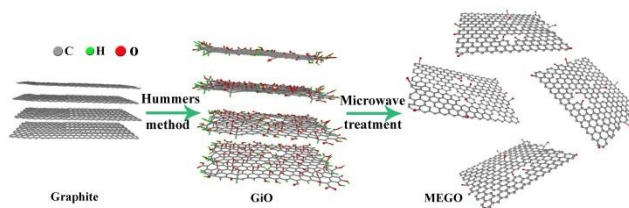
Scheme 1. The formation of MEGO nanosheets.

Synthesis and Characterization of MEGO Nanosheets. The typical preparation of MEGO is illustrated in Scheme 1. As raw material, graphite consisting of close-packed, parallel and nearly defect-free graphitic layers was used. These graphitic layers were expanded by abundant oxygen-containing functional groups on both basal planes and edges, which were generated by the oxidation treatment *via* Hummers' method.[44] This interlayer expansion significantly improves the specific surface area from 30 m^2 g^{-1} for graphite to 70 m^2 g^{-1} for GiO. MEGO was finally obtained through the simultaneous exfoliation and reduction of GiO powders under the exposure of microwave irradiation. The graphitic samples were characterized by elemental analysis, ATR-FTIR, TGA, XRD and Raman (see Part 3, Supporting Information for more details). In short, abundance of oxygen functional groups has been confirmed in the GiO interlayers, which expand the interlayer distance significantly. While barely no oxygen resided in the MEGO nanosheets, resulting in improved electronic conductivity and similar interlayer distance to graphite. Besides, a high quantity of structural defects appears in the MEGO nanosheets. These defects could provide a large number of electrochemically active sites for charge storage on the MEGO nanosheets, which is further discussed in the following section.
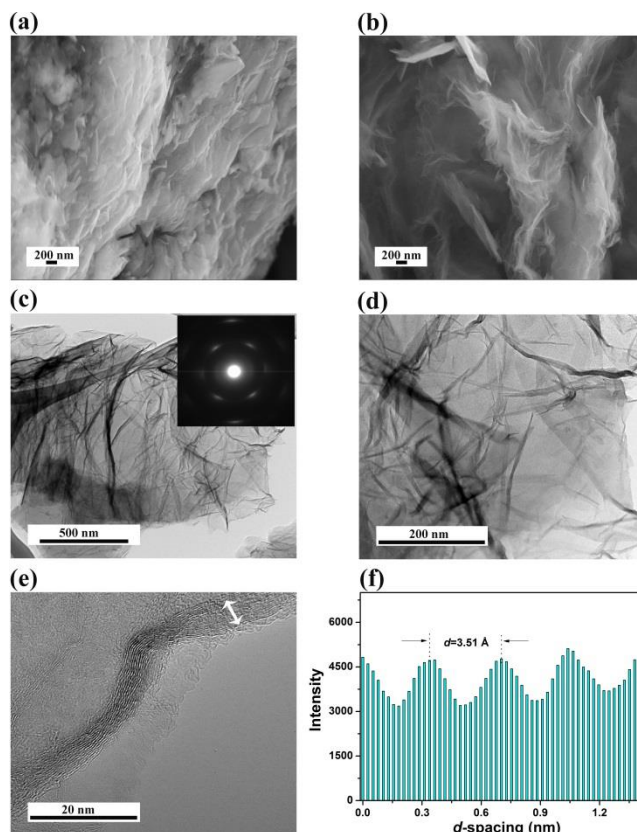
Figure 1. Secondary electron images of (a) graphite and (b) MEGO. (c and d) Typical bright field (BF) TEM images of the MEGO nanosheets. The inset in (c) shows the electron diffraction pattern from the region shown in the BF TEM image. (e) BF TEM image of nanosheets in the MEGO sample where the edge of the nanosheets are bent such that the atomic planes are parallel to the electron beam. (f) The intensity profile across some of the atomic planes that are oriented in cross-section show the interatomic distances.

The morphological features of graphite and MEGO were investigated by FESEM and TEM. The FESEM image in Figure 1a shows that the graphite agglomerates consisted of close-packed graphitic layers. After the oxidation-reduction process, the corrugated and exfoliated nanosheets can be observed in the FESEM image of MEGO (see Figure 1b). Furthermore, the TEM images of MEGO in Figure 1c and 1d, show that the MEGO nanosheets have many crumpled and folded

regions. The selected area electron diffraction (SAED) pattern in the inset has six-fold symmetry. But each of the reflections is elongated into broad arcs, indicating a high defect density with loss of orientational order between each of the atomic layers in the sheet.[45] The graphitic laminar structure of the stacks of MEGO nanosheets could be identified in the 'ordered' region. Figure 1e displays a nanosheet where the edge is bent, showing the atomic layers in cross-section. In Figure 1f, an intensity profile across 4 atomic layers with an average interlayer distance of 3.51 Å is shown. This interatomic distance is similar to the value obtained from the XRD pattern (see Figure S1c).

Based on the above discussion, the combined effect of oxidation, exfoliation and reduction on the graphite powders endows the final product MEGO with a large, conductive and non-perfect hexagonal carbon network. The distinct differences in morphology and structure between graphite, GiO and MEGO should also be evident when applied as cathodes in a Mg battery, which is discussed in the following section.
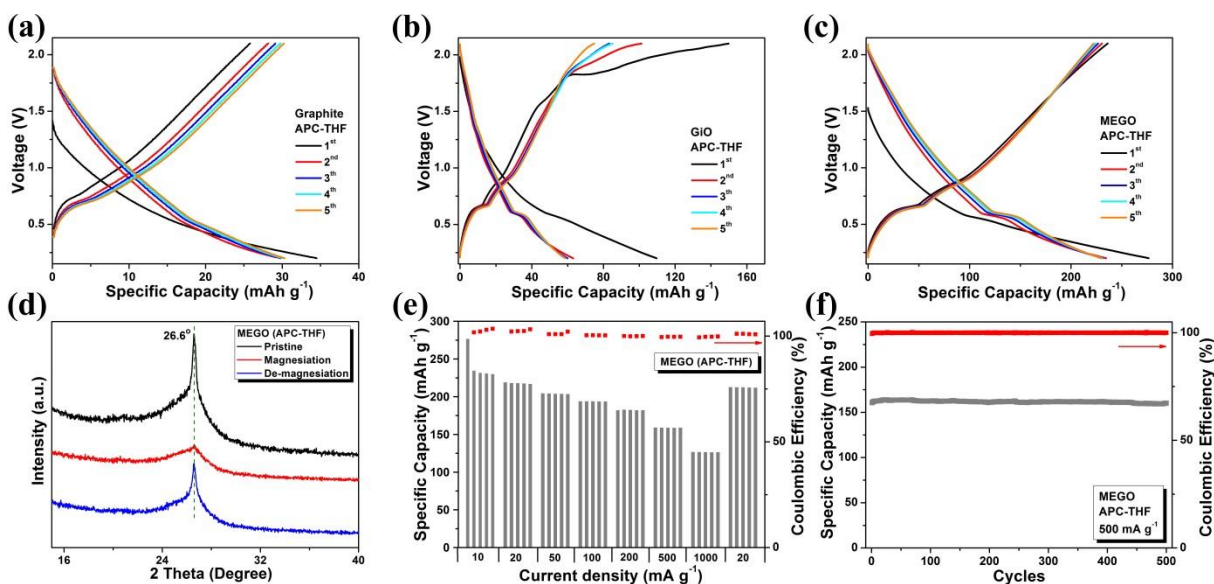
Figure 2. (a-c) Galvanostatic charge/discharge profiles of graphite, GiO and MEGO at 10 mA g^{-1} in APC-THF electrolyte. **(d)** *Ex-situ* XRD patterns of MEGO electrodes at different cell states, cycled at 10 mA g^{-1} in APC-THF electrolyte. **(e)** Rate cyclic performance and **(f)** long cycle life of MEGO cathode in APC-THF electrolyte.

Charge storage mechanism of graphitic cathodes in APC-THF electrolyte. The reversible intercalation/de-intercalation of Mg cations into graphite has been confirmed by *ex-situ* XRD measurements in a recent report of Schmuck *et al.*, where graphite was used as anode and Mg(TFSI)$_2$ as electrolyte. The typical graphite diffraction peak at 26.70° shifted to 26.03° after Mg intercalation. This indicates the expansion of the graphitic layers and the formation of a magnesiated graphite intercalation compound, which also corresponded to the obvious plateaus in the galvanostatic charge/discharge curves.[46] However, neither the wide charge/discharge plateaus nor the shift of the diffraction peak can be observed here. As shown in Figure 2a-2d, the charge/discharge measurements and *ex-situ* XRD analysis of the MEGO cathodes cycled in APC-THF electrolyte do not indicate any Mg intercalation between the MEGO nanosheets. Instead, the

graphitic samples exhibit nearly linear charge/discharge characteristics, which resemble more the behaviour of a capacitor rather than a battery. The absence of Mg intercalation in graphite may be explained by the high charge density of the Mg cations in the APC electrolyte, forming large Mg complexes with the surrounding chloride ions and *esol* molecules.[2,21] The strong coulombic interaction between the Mg^{2+} cations and the surrounding species could possibly lead to only a partial desolvation of the Mg complex at the cathode/electrolyte interface, which makes intercalation rather difficult due to the small space between the graphite layers. Therefore, the reversible capacity of graphite, which is as low as ~30 mAh g^{-1} (see Figure 2a), can be attributed to the capacitive contribution. With the continuously increased surface area from graphite to GiO and MEGO, the reversible capacity increases accordingly. GiO shows a reversible capacity of ~60 mAh g^{-1} (see Figure 2b), while MEGO exhibits the highest reversible capacity of ~230 mAh g^{-1} (see Figure 2c). As a consequence, the capacity of the active electrode is proportional to the surface area. In addition to the high surface area, the defects on the MEGO surface such as vacancies or steps could act as active sites for charge storage,[47,48] and thus contribute to the high capacity observed in MEGO. A capacity loss is observed between the initial discharge and the second discharge for all three samples. This is most likely due to irreversible electrolyte decomposition,[15] which is greatly affected by the surface properties of the cathode. The important effect of the properties of the electrode/electrolyte interface on electrolyte decomposition during the initial cycle is well-established for Li battery systems.[49-51] Similar effects are expected for both Mg batteries and other battery chemistries. Here, for instance, the higher capacity loss in GiO compared with both graphite and MEGO may be caused by the abundant oxygen groups on the surface of the GiO nanosheets. The oxygen groups in GiO can interact with the coordinated THF molecules at the interface, making the charge curves of GiO different from those of graphite and

MEGO in the potential range between 1.5 V and 2.1 V (see Figure 2b). The CV curves of MEGO on different current collectors, which are shown in Figure S2, provide evidence that the high reversible capacities of the MEGO cathode in APC-THF electrolyte originate from the MEGO nanosheets, and not from the Gif current collector.

The important role of Gif was further investigated by analysing the Mg plating-stripping behaviour of the Gif surface in APC-THF electrolyte, and compared with the behaviour of the standard Pt working electrode (WE), please see Part 5, Supporting Information for details. In addition to the Mg stripping/plating, there are also other reactions occurring on the Gif electrode. These are probably caused by the weak Van der Waals interactions between the chlorinated surface of graphite and the $MgCl^+$ complex, which will likely lead to partial desolvation of the Mg complexes at the electrode/electrolyte interface during cycling, and thus provide enhanced capacity. Song *et al.* recently also revealed that the interfacial reactions involving the species of the APC electrolyte (*e.g.* THF solvents) could provide a substantial capacity.[52] In addition, Gewirth *et al.* showed that due to the Lewis acidity of the RMg^+, the THF molecules which are coordinated with the Mg cations at the electrode/electrolyte interface, can be easily oxidized to GBL (γ-butyrolactone).[53,54] There may be other concurrent electrochemical reactions as well taking place at the interface. For example, during the oxidation of THF to GBL, the intermediate products 2-hydroxytetrahydrofuran,[55] 2,2-dihydroxytetrahydrofuran[56] and THF peroxide[57,58] could coexist. Also, ring-opening of THF molecules initiated by the catalysis of Al^{3+}/ Mg^{2+} metal cations may occur.[52,54,55,59] All of these chemical reactions make the analysis of the products of the interfacial reactions very complicated. A complete and detailed understanding of all possible interfacial reactions, which is beyond the scope of this work, is still lacking due to the complexity of the APC electrolyte according to the studies reported by Aurbach *et al.*.[15]

Nevertheless, these little-known *esol*-related reactions at the interface in our cell seem to be reversible based on the *ex-situ* XRD patterns of the MEGO electrodes at different cell states (see Figure 2d). It is clearly seen that the peak intensity decreases significantly for the magnesiated MEGO electrode compared with the pristine and de-magnesiated material. This change in intensity may be attributed to the formation of various products generated by the interfacial reactions, both organic and inorganic. These products would weaken the XRD signal from the MEGO underneath. The peak intensities recovered during the de-magnesiation process, showing that the loss of intensity of the XRD signal was not related to salt or solvent residues left on the surface. This periodic change in XRD peak intensities, also observed in the Mn_3O_4-APC-THF system,[25] illustrates a high magnesiation/de-magnesiation efficiency. This provides the high rate capabilities and high cycling stability of the MEGO cathode, as shown in Figure 2e and 2f, respectively. Figure 2e shows that MEGO exhibits excellent rate performance at various current densities from 10 mA g^{-1} to 1 A g^{-1}. Except for the initial irreversible capacity loss at 10 mA g^{-1}, no capacity loss and almost 100 % coulombic efficiencies were observed during the 5 cycles at each current density. The capacities of MEGO are 230, 204 and 194 mAh g^{-1} at the current densities of 10, 50 and 100 mA g^{-1}, respectively. These values are much larger than that reported for fluorinated graphene, another similar carbonaceous cathode (110 mAh g^{-1} at 10 mA g^{-1}, 90 mAh g^{-1} at 50 mA g^{-1}, and 50 mAh g^{-1} at 100 mA g^{-1}).[21] MEGO maintains ~55% of its initial specific capacity as the current density increases from 10 mA g^{-1} to 1 A g^{-1}. After charge/discharge at a high rate of 1 A g^{-1}, the capacity fully returns to the initial value when the battery is cycled at 20 mA g^{-1} again. Extended cycling performance is a key factor in determining the suitability of the battery electrodes for practical applications. As shown in Figure 2f, MEGO displayed 100% coulombic efficiency and 100% capacity retention after 500 cycles at 500 mA g^{-1}.
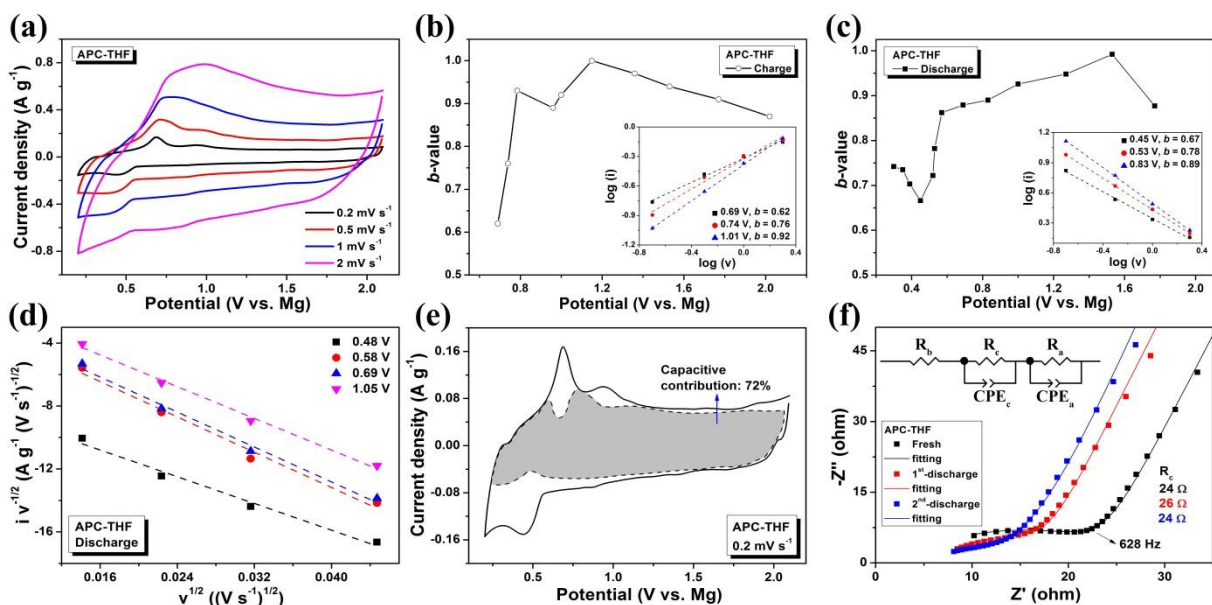
Figure 3. (a) CV curves of MEGO at different scan rates. Dependence of *b*-values as a function of potential for **(b)** anodic sweeps and **(c)** cathodic sweeps. Insets: power law dependence of current as a function of sweep rate. **(d)** Plots of $v^{1/2}$ vs i $v^{-1/2}$, v varies from 0.2 to 2 mV s^{-1}. **(e)** The capacitive contribution (the shaded region) to the total stored charge at 0.2 mV s^{-1}. **(f)** The high-frequency region of the Nyquist plots of MEGO electrodes at different cell states under 10 mA g^{-1} in the frequency range of 10^4 Hz to 0.01 Hz. Inset: equivalent circuits of the MEGO cathode in APC-THF electrolyte.

Kinetics and quantitative analysis of the MEGO cathode in APC-THF Electrolyte. To further understand the charge storage mechanism and explain the high rate capability and high cycling stability of the MEGO cathode in APC-THF electrolyte, it is necessary to perform a kinetics analysis in the potential range that covers the cathodic/anodic peaks, following the method proposed by Lindquist *et al.* (see Part 6, Supporting Information for details).[60] As shown in Figure 3a-3c, the *b*-values of the anodic peak at 0.69 V and the cathodic peak at 0.45 V are 0.55 and 0.67, respectively, indicating that the interfacial redox reactions involving THF molecules are diffusion-

14

controlled. Similar behaviour has been reported by Conway *et al.*, showing that the redox reactions can be diffusion controlled if the redox reactants constitute the solution species.[61] On the other hand, the *b*-values for the potentials above the apparent peaks are higher than 0.8, indicating that capacitive processes are governing. Thus, it seems reasonable to conclude that the total stored charge in the MEGO nanosheets originates from both diffusion-controlled *esol*-related interfacial reactions and non-diffusion controlled capacitive processes.

The fraction of these two contributions can be quantified according to the linear plot of $v^{1/2}$ vs i $v^{-1/2}$ in Figure 3d (see Part 6, Supporting Information for details).[39] As shown in Figure 3e, the contribution from the capacitive effect, which corresponds to the shaded area of the CV curve, accounts for ~72% of the total stored charge, governing the charge storage mechanism in the MEGO-APC cell. This capacitive contribution becomes more prominent with increased scan rate, which is seen by the more rectangular shape of the CV curves in Figure 3a. As a consequence, the charge storage mechanism observed for the MEGO nanosheets resembles more that of a supercapacitor rather than a battery. In a conventional Mg-ion battery the charge/discharge processes are limited by slow diffusion of metal cations in the solid state, while in the current case the capacities are determined by the transfer of ions and electrons along the surface of the active material. This leads to a relatively low and stable charge transfer resistance (R_c) at the interface of the MEGO cathode/APC electrolyte, which can be seen in the fitted Nyquist plots at high frequencies. The proposed equivalent circuit is given in the inset of Figure 3f. Here, R_b is the bulk resistance of the assembled cell, and R_a is the charge transfer resistance at the interface of the Mg anode/electrolyte, corresponding to the large semicircle at medium and low frequency ranges (see Figure S6).[62] Hence, these findings make it reasonable to conclude that the MEGO-APC-THF cell system seems to be governed by the capacitive processes and exhibits relatively low interfacial

resistance during cycling. This may account for the excellent rate performance (see Figure 2e) and high cycling stability (see Figure 2f) of the MEGO cathode in APC electrolyte. The fact that capacitive processes govern the charge/discharge mechanism makes the surface area and morphological features of the active material vital factors for cell performance. This is also nicely displayed in the results, where the MEGO nanosheets exhibit significantly higher capacities than both graphite and GiO. MEGO nanosheets are shown to have substantially higher surface areas than the latter two, and possess more structural defects which are able to facilitate fast surface reaction kinetics.

In short, based on the above mechanism and kinetics analyses of the MEGO cathode in APC electrolyte, the total stored charge in the MEGO nanosheets is found to stem from a combination of capacitive processes and *esol*-related interfacial reactions. Both of these two contributions occurred at the electrode/electrolyte interface and are closely related to the structure of the Mg monomers, which determines the charge transfer across the interface.[36,63] The *esol* molecules have a dramatic effect on the formation of the Mg monomers and seem to control the interfacial reactions. The chemical nature of the interfacial reactions will to a large extent determine the cell performance since they could significantly alter the electrochemical activity of the electrolyte.[47] Some of the reactions are beneficial for the cell performance, such as in the MEGO-APC-THF system investigated here. Whereas, other reactions can reduce the stability of the electrolyte and lower the cell performance, which is the case for the ion-blocking amorphous layer in the MnO_2-Mg(HMDS)-THF system.[42,64] Thus, to further develop the Mg battery, it is essential to investigate and utilize these interfacial reactions. With this purpose in mind, several other chain-type *esol*s have been used to replace the ring-structured THF solvent in the APC electrolyte in order to study the important role of the *esol*s in the interfacial reactions. These include DME, G2 and G4, which

all show a similar chain structure but with different chain lengths ($CH_3O(CH_2CH_2O)_nCH_3$ (n equals to 1 for DME, 2 for G2 and 4 for G4), see Scheme 2).
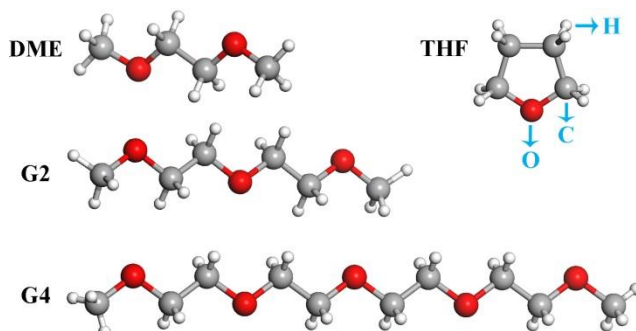
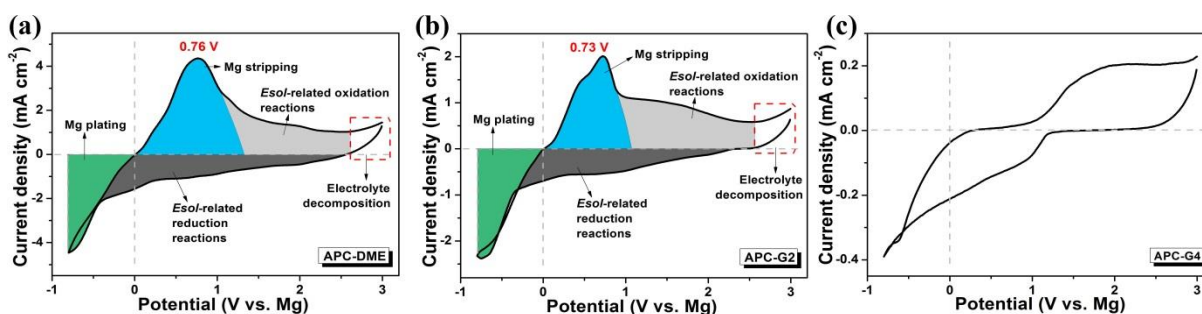**Scheme 2. The molecular structures of THF, DME, G2 and G4.**

Figure 4. CV curves of Mg deposition/stripping at 10 mV s^{-1} in (a) APC-DME, (b) APC-G2 and (c) APC-G4 electrolytes. Experiments are conducted on a Gif working electrode with a Mg metal as reference and counter electrode.

The effect of *esol*s on the cell performance. As shown in Figure 4, Mg deposition/stripping can be observed in APC electrolytes with chain-typed *esol*s. Although the behaviour of the APC-G4 electrolyte seems to deviate from the other two electrolytes, indicating limited or no Mg stripping/deposition. The Mg deposition/stripping in both APC-DME and APC-G2 electrolytes occur at approximately the same potentials as in the APC-THF electrolyte (see Figure S3). However, additional reactions can also be observed. The proportions of the areas that represent the

interfacial reactions to the whole area of the CV curve are found to be significantly larger in APC-DME and APC-G2 electrolytes than in APC-THF electrolyte (see Figure S3b). The different electrochemical responses in APC electrolytes with different structured *esol*s do indeed demonstrate the crucial role of *esol*s for the electrochemical behaviour at the electrode/electrolyte interface, which directly determine the charge storage performance of the electrodes.

Looking into the charge/discharge mechanisms of the MEGO nanosheets in electrolyte with chain-type *esols*, it bears strong resemblance to the behaviour observed in the APC-THF electrolyte. The *ex-situ* XRD characterization (see Figure S7) shows no change in peak positions for any of the three electrolytes (APC-DME, APC-G2 and APC-G4) upon cycling, indicating that there is still no intercalation of Mg ions between the graphite sheets. The kinetics analyses according to Lindquist's procedure[60] are also performed here (see Figure S8). For all three electrolytes, the charge processes seem to be mostly non-diffusion controlled as the majority of the *b*-values are in the range of 0.8-1. The discharge processes on the other hand, behave somewhat differently. For the solvents DME and G2, the discharge seems to start as mostly non-diffusion controlled at higher voltages. Around a certain potential the *b*-values drop rapidly, transitioning the discharge process into a more diffusion controlled regime. The *b*-values also drop with decreasing potential for the G4 solvent. However, the transition away from the non-diffusion controlled regime is more gradual. And the *b*-values for the G4 solvent are much higher than that of the DME and G2 solvents at lower potentials, indicating that the longer chained molecules favour more non-diffusion controlled processes. As a result, the various kinetics of the MEGO cathodes in APC electrolytes reveal that the *esol*s of the APC electrolytes with different molecular structures could alter the electrochemical activities at the electrode/electrolyte interface.
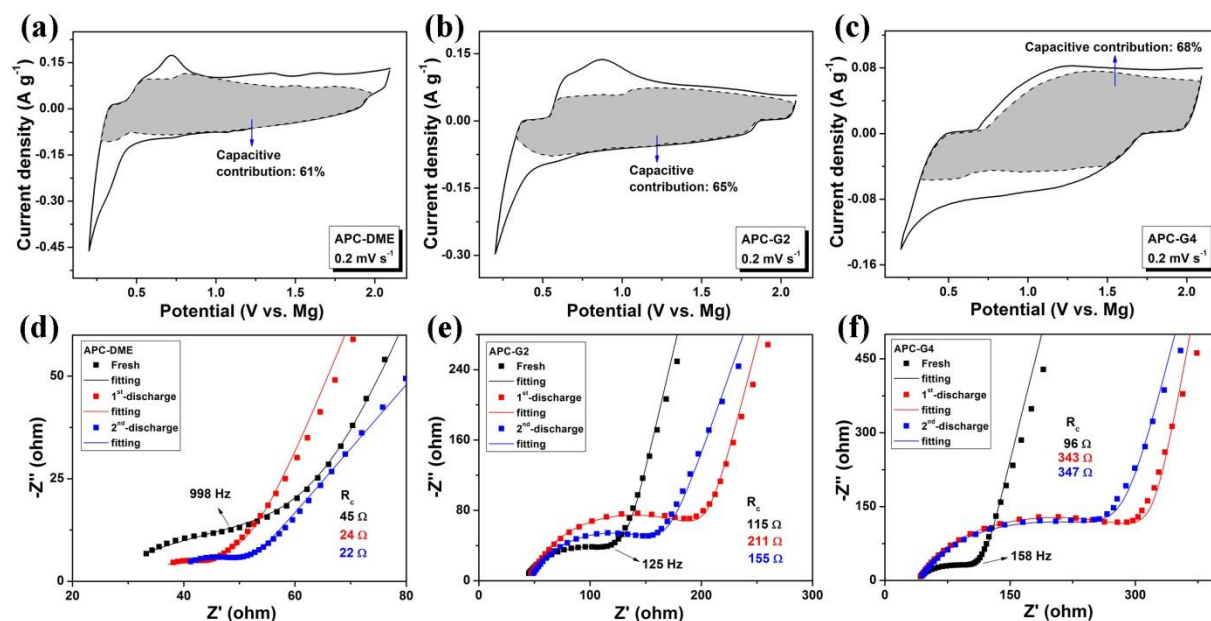
Figure 5. The capacitive contribution (the shaded region) to the total stored charge of the MEGO nanosheets in (a) APC-DME, (b) APC-G2 and (c) APC-G4 electrolytes. The high-frequency region of the Nyquist plots of MEGO electrodes at different cell states in (d) APC-DME, (e) APC-G2 and (f) APC-G4 electrolytes. The EIS data are fitted by using the same equivalent circuits as in the APC-THF electrolyte (inset in Figure 3f).

Also, the contributions from both the capacitive processes and the diffusion controlled reactions involving *esol*s have been quantitatively analysed according to the linear plot of $v^{1/2}$ vs i $v^{-1/2}$ shown in Figure S9. In accordance with the kinetics analysis, the capacitive contribution to the total stored charge of the MEGO nanosheets in electrolytes with longer chain length (APC-G4, see Figure 5c) is slightly higher than that observed in electrolytes with shorter chain lengths (APC-DME, see Figure 5a and APC-G2, see Figure 5b). Interestingly, with the increased chain lengths, from DME to G4, the capacitive contributions and the interfacial resistances (see Figure 5d-5f and Figure S10) increased. Compared with G2 and G4 solvents, the DME solvent with the shorter chain-length provide relatively lower charge transfer resistance and a lower capacitive contribution. This may

indicate that there is a geometric effect where the shorter chain molecules are able to more readily approach the active sites for interfacial reactions compared with the long chain molecules. Thus, the contribution from the diffusion-controlled reactions as well as the total charge stored will increase. With the increased chain length on the other hand, the interfacial reactions involving the *esol*s will be more complex. This may be a geometric effect, but there are also more reactive sites in the longer chain molecules due to the increasing number of oxygen atoms in the chain, as illustrated in Scheme 2. More oxygen on the chain leaves the possibility of forming several other Mg complex derivatives, and thus complicates the interfacial reactions and the corresponding products formed on the surface of the electrode. The magnesiation process in APC electrolyte is roughly illustrated in Scheme 3. The Mg cations in the Mg monomers adsorb on the surface of the electrode, providing the capacitive contribution, while the coordinated electrolyte species are involved in the interfacial reactions, resulting in the formation of a product layer on the electrode surface. This product layer, *e.g.* in APC-DME electrolyte, is confirmed to be non-conducting and mainly consist of a polymeric Mg^{2+} complex with solvent coordination according to the *ex-situ* ATR-FTIR analysis (see Part 11, Supporting Information for details). As a consequence, charge is stored due to the generation of a large interfacial dipole. The main challenge with a charge storage mechanism as suggested here is that the charge storage collapses as soon as the respective electrode is removed from the electrolyte. After disconnecting the electrodes, the state of the electrode surface relaxes to open circuit conditions, with large associated changes of the interfacial capacitance, *i.e.* the stored charge. In a way, the absence of significant organic films on the carbon surface in the charged state detected by IR spectroscopy confirms the assessment of a mainly capacitive interfacial charge storage, even though it is not quantitative *e.g.* as to molecular orientation of species near the interface. Compared to DME, the longer chain *esol*s (*e.g.* G2 and

G4) complicate the chemical system of the product layer and dramatically increase the interfacial resistances and potentially passivate the electrode surface, which may hinder the interfacial reactions for the following cycle. This would also make the magnesiation process more controlled by capacitive processes compared with the shorter chain *esol*s. As a consequence, compared with the DME molecules, the G2 molecules with relatively longer chain length would significantly increase the interfacial resistances that include both the cathode/electrolyte interface and anode/electrolyte interface. The high interfacial resistances result in a lower response current that corresponds to a lower capacity in APC-G2 electrolyte than that in APC-DME electrolyte. Furthermore, the G4 molecules with the longest chains give rise to extremely high interfacial resistances, as shown in Figure 5f and Figure S10c. Such high interfacial resistances may also be the main reason for the lack of Mg plating/stripping shown in Figure 4c. It indicates that the interfacial reactions are different from those in the other three investigated electrolytes (APC-THF, APC-DME and APC-G2). In the THF solvent, however, low MEGO/electrolyte interfacial resistance and high capacitive contribution are observed. It has previously been found that both the ring-structured (THF) and chain-structured (DME, G2 and G4) *esol* molecules adsorb parallel to the surface plane of the cathode.[47] As a result, it seems reasonable that the chain length as well as molecule structure should play an important role in interfacial properties, and contribute to the cell performances. This was further studied by galvanostatic measurements, as shown in Figure 6 and Figure 7.
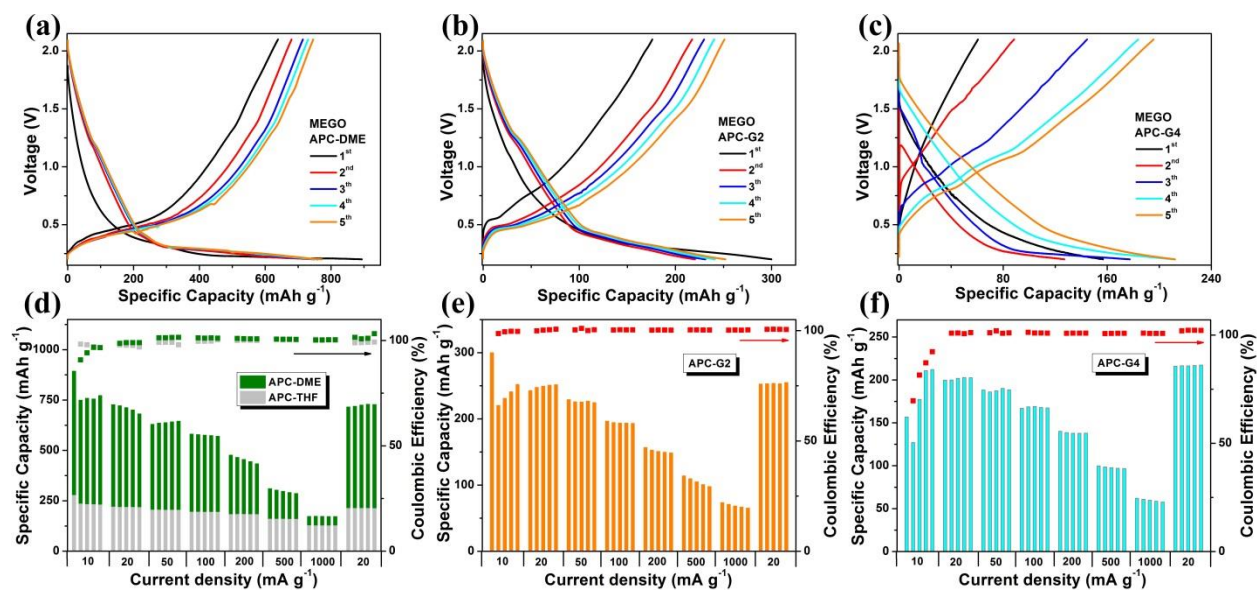
Figure 6. Galvanostatic charge/discharge profiles (at 10 mA g⁻¹) and rate cyclic performance of MEGO in (a,d) APC-DME, (b,e) APC-G2 and (c,f) APC-G4 electrolytes, respectively.
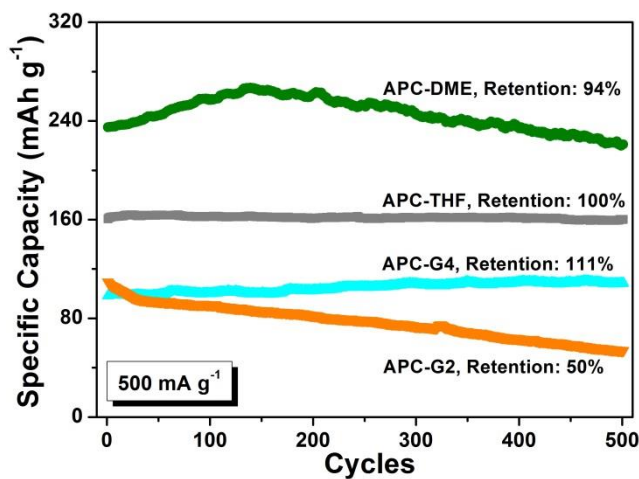

Figure 7. Long cycle life of MEGO at 500 mAh g⁻¹ in APC electrolytes with different *esol*s.

In Figure 6a-6c, all the cells were charged at the same current density of 10 mA g⁻¹ and in the same potential range of 0.2 - 2.1 V. In the APC electrolyte with a short-chain DME solvent, MEGO

shows a high initial capacity close to 900 mAh g^{-1} at 10 mA g^{-1}. There is an irreversible capacity loss after the first cycle, but the capacity seems to stabilize around 780 mAh g^{-1} from the 2nd cycle onward (the capacity of Gif is negligible in APC-DME electrolyte[65]). This value is more than 3 times the capacity obtained in the APC electrolyte with THF as the solvent. It is also, to the best of our knowledge, the highest reversible capacity reported for any Mg battery cathode when considering metal oxides,[30,66-68] silicates,[69] sulfides,[32,70] selenides,[71,72] carbon allotrope[21,73] and organic-based materials.[74,75] In addition, as shown in Figure 6d, no permanent capacity loss is observed after cycling at 1 A g^{-1}, and the capacity fully recovers to 720 mAh g^{-1} at 20 mA g^{-1}, compared with 710 mAh g^{-1} at initial 20 mA g^{-1}. The obtained capacities seem to depend on the chain length, which decides the interfacial resistance. Hence, compared with DME, G2 (medium chain) provides a cell with higher charge transfer resistance and a modest reversible capacity of ~250 mAh g^{-1} at 20 mA g^{-1}, while G4 (longest chain) gives a system with even higher charge transfer resistance, and thus shows the lowest reversible capacity of all the four electrolytes investigated (~200 mAh g^{-1} at 20 mA g^{-1}). The MEGO cathode also exhibits very different cycling stability in combination with the various electrolyte solvents. As shown in Figure 7, after 500 cycles at a current density of 500 mA g^{-1}, 100%, 94%, 50% and 111% of the initial capacity was retained in APC-THF, APC-DME, APC-G2 and APC-G4, respectively.
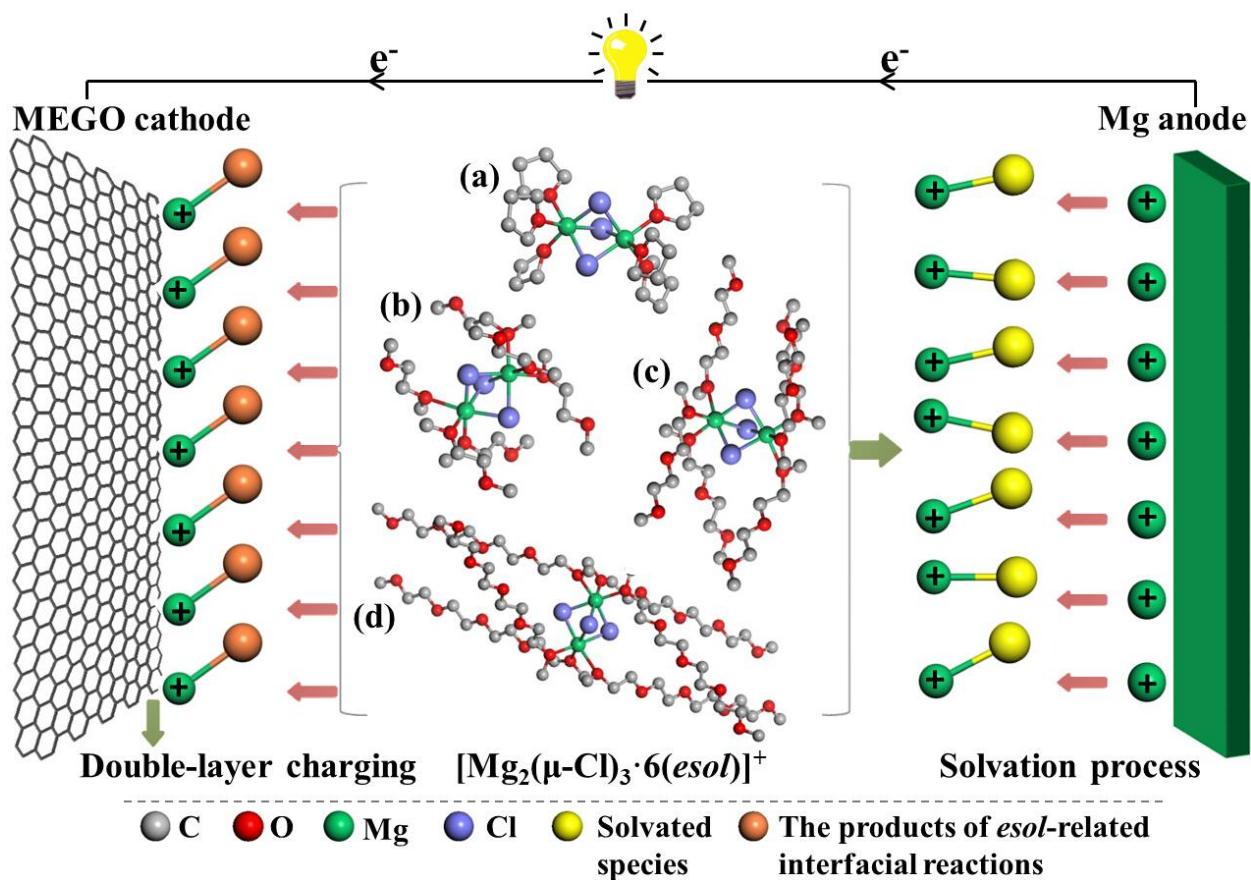
Scheme 3. Magnesiation process in APC electrolytes and molecular structures of [Mg$_2$(μ-Cl)$_3$·6$esol$]$^+$, where $esol$ is (a) THF, (b) DME, (c) G2 and (d) G4, respectively.
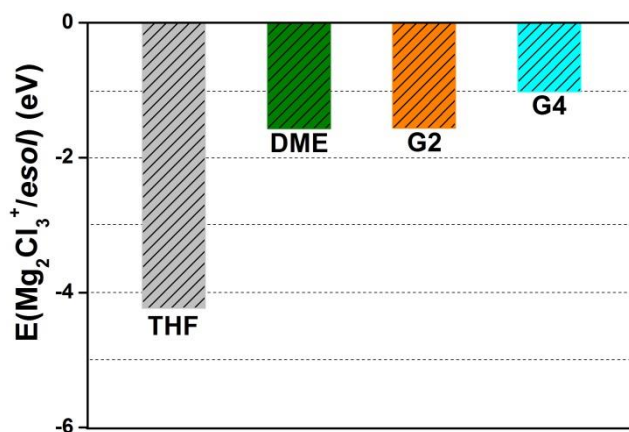

Figure 8. Calculated interaction energies between Mg$_2$Cl$_3^+$ and the coordinating $esol$ molecules in the solvent system.

Interactions energies between Mg$_2$Cl$_3^+$ and *esol*s. To further understand the distinction between the APC electrolytes caused by the different *esol*s, we have calculated the interaction energies $\Delta E(Mg_2Cl_3^+/esol)$ of Mg$_2$Cl$_3^+$ with the *esol* (see Part 12, Supporting Information for details). The calculated values of the interaction energies are shown in Figure 8 and the molecular structures of the Mg dimers are illustrated in Scheme 3. Due to the many similarities between these APC electrolytes, we assume that the Mg dimers with the chain structured *esol* molecules all have the same coordination number with $[Mg_2(\mu\text{-}Cl)_3\cdot6THF]^+$. In APC electrolytes, the *esol* molecules stabilize the Mg$_2$Cl$_3^+$ complex through Mg-*esol* coordination. Figure 8 shows the relatively stronger interaction energies of Mg$_2$Cl$_3^+$ with THF molecules compared with the other three chain-typed *esol* molecules, illustrating that the Mg dimers with ring-structured THF molecules are more stable in the APC electrolyte. The strong interaction between the Mg$_2$Cl$_3^+$ ions and the coordinated THF molecules makes the electrolyte more stable, and less prone to irreversible oxidation/reduction of *esol*s. This also leads to a charge storage mechanism controlled by capacitive processes and low interfacial resistance, explaining the high rate capability and excellent cycling stability observed for the MEGO cathode in APC-THF electrolyte. The relatively weaker interaction of the Mg$_2$Cl$_3^+$ with both DME molecules and G2 molecules, associated with their short-chain structure, facilitated *esol*-related reactions at the interface of the cathode/electrolyte. Thus, the strong redox peaks appearing in the CV curve of the MEGO cathode in both these two electrolytes is attributed to diffusion-controlled reactions. The charge storage performance of the MEGO cathode, including the rate capability and cycling stability, is closely related to the interfacial reactions governed by the *esol* structure. With the extended chain length, the G4 molecules show the weakest interaction with Mg$_2$Cl$_3^+$. The unstable Mg-G4 complex facilitates numerous interfacial reactions, which seem to passivate the electrode surface, as

discussed above. This would allow for the magnesiation process to be governed mainly by capacitive processes. It should be noted that the model used here considers only one possibility for the Mg dimers with G2 (or G4) molecules and the coordination number of the Mg dimers with chain structured *esol*s are assumed to be six. Realistically, the APC electrolytes with chain structured *esol*s, especially for G2 and G4 solvents, tend to be more complex. The increased complexity stems from both the increasing number of oxygen atoms in the solvent molecule chain, and from the fact that the coordination number of the Mg dimers may vary depending on the structure of the *esol* (ring or chain). In theory, both these two factors are supposed to be taken into consideration for an accurate description of the interaction between $Mg_2Cl_3^+$ and the coordinated *esol* molecules. The calculations here can be regarded as a step towards a general understanding of the influence of different *esol*s on the APC electrolytes. Nevertheless, it is reasonable to conclude that the *esol* molecule structure will affect the chemical nature of the diffusion-controlled reactions at the electrode/electrolyte interface, and thereby determine the nature and reversibility of the charge/discharge reactions.

Conclusions

In this work, we have investigated a Mg battery consisting of a carbonaceous cathode, Gif current collector, APC electrolyte and Mg metal anode. This cell concept avoids the challenges with sluggish solid-state diffusion of Mg^{2+} cations into a host lattice or intercalation into conventional graphite. The charge stored in the MEGO nanosheets mainly stems from fast capacitive processes and reversible interfacial reactions, which are controlled by the electrolyte solvents. MEGO nanosheets display the highest reversible capacity among any reported cathodes for Mg batteries, along with excellent cycling stability in APC-DME electrolyte. There are still unanswered questions regarding details of all the chemical reactions taking place during cycling. And much

more research is necessary to gain a complete understanding of these systems, which will be required to fully exploit their potential. However, we believe these results point in a promising direction for developing better Mg batteries.

Methods/Experimental

Synthesis of MEGO. Graphite oxide (GiO) powders were prepared by a modified Hummers' method.[44] In a typical process, natural graphite (Alfa Aesar, 99.9 %) was treated sequentially with concentrated H_2SO_4 (Alfa Aesar, 95-98 %), KNO_3 (Alfa Aesar, 99 %) and $KMnO_4$ (Alfa Aesar, 98 %). Subsequently, water was added into the mixture under vigorous stirring. Afterwards, H_2O_2 (Alfa Aesar, 35 wt. % in H_2O) solution and water were added sequentially to dissolve insoluble manganese species. The resulting GiO suspension was filtered and washed using dilute HCl solution (Alfa Aesar, 5 wt. % in H_2O). The colloidal GiO was obtained and dried under vacuum. The resulting product was ground into powder (100 mesh). Further treatment of GiO powders to MEGO was performed according to the same procedure reported by Ruoff's research group.[43] Briefly, GiO powders were first irradiated in a microwave oven (Wilfa, Model WP800L20) in ambient conditions at 700 W for 1 min. Black and fluffy MEGO powders were obtained after a large volume expansion of the GiO powders due to the microwave irradiation. Commercially available graphite (Alfa Aesar) was used without further treatment to study the effect of morphology features and surface area on the battery performance as Mg battery cathode material.

Preparation of electrolyte. The APC-THF electrolyte solution was synthesized according to a previously described procedure.[2] The Lewis base, phenylmagnesium chloride in tetrahydrofuran solution (PhMgCl in THF, Aldrich, 99%) was mixed with the Lewis acid, aluminium trichloride ($AlCl_3$, Aldrich, 99.999%) in THF solution (Aldrich, anhydrous) with a molar ratio of 2:1. The

concentration was 0.4 mol L^{-1} for this study. The obtained solution was stirred at least 24 hours prior to use. All activities were performed in an Ar-filled glove box (< 0.1 ppm of water and oxygen), since the electrolyte is moisture sensitive.

The synthesis of APC electrolytes with other *esol*s (DME (Alfa Aesar, 99+%), G2 (diglyme, Aldrich, anhydrous) or G4 (tetraglyme, Aldrich, 99+%)) was performed by further treatment of the APC-THF electrolyte. First, the synthesized APC-THF electrolyte was evaporated under vacuum at ambient temperature overnight. A white precipitate was obtained after complete evaporation of the THF solvent. Then the necessary amount of *esol* was introduced to dissolve this white precipitate followed by stirring overnight.

Material Characterization. XRD studies were performed on a Bruker AXS D8 FOCUS diffractometer with Cu Kα radiation and a Lynxeye detector. Brunauer-Emmett-Teller (BET) surface areas were obtained from N_2 adsorption isotherms measured at liquid nitrogen temperature with a Micrometrics Tristar 3000 instrument. Before the measurements, the samples were degassed at 120 □C under vacuum overnight to eliminate adsorbed water. ATR-FTIR analyses of GiO and MEGO were performed with a Bruker Optics IFS66V S-1 spectrometer, where a microscope (HYPERION 3000) was fitted with an ATR objective as the internal reflectance element and a mercury-cadmium-telluride (MCT) detector. The number of scans was 68, and the scanning resolution was 2 cm^{-1}. IR spectroscopic analysis of electrodes in the charged and discharged states was done on a Bruker Vertex 80v spectrometer with a Platinum ATR unit containing a diamond ATR crystal. Electrode sheets were fixed on the spectrometer's crystal plate in a glove box and sealed air tight, after a reference measurement with the blank crystal was obtained. Spectral resolution was 4 cm^{-1}. Raman spectroscopy measurements were performed on a micro-Raman system (Renishaw, DM2500-In Via) with excitation energy of 2.41 eV (514 nm). Raman spectra

were taken by depositing the powder samples on a glass slide. The thermal properties of the samples were characterized by thermogravimetric analysis (TGA) (Netzsch STA 449C). Measurements on both Graphite and MEGO were performed under flowing nitrogen gas (flow rate of 30 ml min^{-1}) and over a temperature range from room temperature to 800 °C with a ramp rate of 10 °C min^{-1}. The GiO sample was also heated from room temperature to 800 °C at 1 °C min^{-1} to avoid thermal expansion of the GiO due to rapid heating. The morphology of the products was studied using field emission scanning electron microscopy (FESEM, Zeiss Ultra, 55 limited Edition) and transmission electron microscopy (TEM) (double Cs corrected coldFEG JEOL-ARM200CF, operated at 200 kV). The electrical conductivity of the powder samples (σ_E) was measured by using a Kelvin bridge[76] and calculated according to the following equation:

$$\sigma_E = [R_{measured}\frac{S}{H}]^{-1}$$

$R_{measured}$ is the measured electrical resistance (0.01 $\mu\Omega$ - 1000 Ω), S and H are the cross section and height of the powder column, respectively.

Electrochemical Measurements. The cathode was prepared by mixing 90 wt% of the sample and 10 wt% of polyvinylidene difluoride (PVDF, Kynar, reagent grade) in the presence of N-methyl pyrrolidinone (NMP, Aldrich, >99%). The slurry was made by ball milling, followed by drop coating onto flexible Gif (graphite foil, Goodfellow, 99.8%). The electrodes were dried at 120 ºC under vacuum for 10 hours. After that, the dried film was punched into discs with 16 mm diameter. The mass loading of the electrode is about 0.45 mg. The electrochemical performance of the active materials was examined via CR2016 coin cells with a 0.2 mm thick Mg ribbon counter electrode, glass microfiber separator (Whatman), and 0.4 mol L^{-1} APC electrolyte. Before use, the Mg ribbon was polished on both sides with SiC paper, followed by etching in chromic acid for 2

mins, then washed clean with THF and dried overnight under vacuum. The cells were assembled in an Ar-filled glove box. Galvanostatic charge/discharge testing was performed at ambient temperature on a Maccor 4200 (Maccor Inc., USA) battery testing system with cut-off voltages of 2.1/0.2V vs. Mg. The current densities varied from 10 mA g^{-1} to 1 A g^{-1}. The electrochemical impedance spectra (EIS) were obtained by using the coin cell configuration on a Gamry Reference 600 instrument (Pennsylvania, USA) under the frequency range of 0.01 Hz-10 kHz and 5 mV of AC perturbation. The collected EIS data were fitted by using ZView software. CV measurements of the cathodes were performed at potentials between 0.2 and 2.1 V vs Mg, using a 3-electrode cell (EL-CELL) with Mg ribbon as both reference- and counter electrode, by Gamry Reference 600 instrument.

Computational details for the calculations of interactions energies between Mg$_2$Cl$_3^+$ and *esol*s. First principles calculations were performed with the Vienna *Ab initio* Simulation Package (VASP)[77,78] using the PBEsol functional.[79,80] The standard PBE PAW potentials C ($2s^2 2p^2$), H ($1s^1$), O ($2s^2 p^4$), Mg_pv ($2p^6 3s^2$) and Cl ($3s^2 3p^5$) potentials supplied with VASP were used and plane waves were expanded up to a cut off energy of 500 eV. Brillouin zone integration was done on a single gamma-centred k-point for calculations, and the forces on the ions were relaxed until they were below 0.01 eV Å^{-1}. Solvation calculations were performed by using the continuum solvation model VASPsol throughout this work.[81,82] Solvent dielectric constants were set to 7.58 for THF, 7.2 for DME, 7.23 for G2 and 7.79 for G4. In order to assess the interaction energies of Mg$_2$Cl$_3^+$ with THF, DME, G2 or G4 molecules, large unit cells with 20×20×20Å, 20×20×20Å, 22×22×22Å or 35×35×35Å frame, respectively, were used to avoid the long-range interactions due to the periodic boundary conditions.

AUTHOR INFORMATION

Corresponding Author

*E-mail: fride.vullum-bruer@ntnu.no

ASSOCIATED CONTENT

Supporting Information.

Part 1. Chemical System of APC Electrolyte; Part 2. Materials Characterizations; Part 3. CV Curves of MEGO Electrodes on Different Current Collectors; Part 4. Analysis of Mg Plating/Stripping on the Surface of Pt or Gif; Part 5. Kinetics and Quantitative Analyses Method; Part 6. Nyquist Plots of MEGO Electrodes in APC-THF Electrolyte; Part 7. *Ex-situ* XRD Characterizations of MEGO Electrodes in Different APC electrolytes; Part 8. Kinetics and Quantitative Analyses of MEGO Electrodes in Different APC Electrolytes; Part 9. Nyquist Plots of MEGO Electrodes in Different APC Electrolytes; Part 10. *Ex-situ* ATR-FTIR Characterization of MEGO Electrodes in APC-DME Electrolyte; Part 11. Analysis of Stability of Mg Dimers with Different *Esol*s.

REFERENCES

(1)   Levi, E.; Gofer, Y.; Aurbach, D. On the Way to Rechargeable Mg Batteries: The Challenge of New Cathode Materials. *Chem. Mater.* **2010**, *22,* 860-868.

(2)   Yoo, H. D.; Shterenberg, I.; Gofer, Y.; Gershinsky, G.; Pour, N.; Aurbach, D. Mg Rechargeable Batteries: An on-Going Challenge. *Energy Environ. Sci.* **2013**, *6,* 2265-2279.

(3)   Aurbach, D.; Cohen, Y.; Moshkovich, M. The Study of Reversible Magnesium Deposition by *in Situ* Scanning Tunneling Microscopy. *Electrochem. Solid-State Lett.* **2001**, *4,* A113-A116.

(4)   Xu, K. Nonaqueous Liquid Electrolytes for Lithium-Based Rechargeable Batteries. *Chem. Rev.* **2004**, *104,* 4303-4417.

(5)   Liang, Y.; Yoo, H. D.; Li, Y.; Shuai, J.; Calderon, H. A.; Robles Hernandez, F. C.; Grabow, L. C.; Yao, Y. Interlayer-Expanded Molybdenum Disulfide Nanocomposites for Electrochemical Magnesium Storage. *Nano Lett.* **2015**, *15,* 2194-2202.

(6)   Ling, C.; Banerjee, D.; Matsui, M. Study of the Electrochemical Deposition of Mg in the Atomic Level: Why it Prefers the Non-Dendritic Morphology. *Electrochim. Acta* **2012**, *76,* 270-274.

(7)   Muldoon, J.; Bucur, C. B.; Oliver, A. G.; Sugimoto, T.; Matsui, M.; Kim, H. S.; Allred, G. D.; Zajicek, J.; Kotani, Y. Electrolyte Roadblocks to a Magnesium Rechargeable Battery. *Energy Environ. Sci.* **2012**, *5,* 5941-5950.

(8)   Muldoon, J.; Bucur, C. B.; Gregory, T. Quest for Nonaqueous Multivalent Secondary Batteries: Magnesium and Beyond. *Chem. Rev.* **2014**, *114,* 11683-11720.

(9)   Doe, R. E.; Han, R.; Hwang, J.; Gmitter, A. J.; Shterenberg, I.; Yoo, H. D.; Pour, N.; Aurbach, D. Novel, Electrolyte Solutions Comprising Fully Inorganic Salts with High

Anodic Stability for Rechargeable Magnesium Batteries. *Chem. Commun.* **2014**, *50,* 243-245.

(10)   Keyzer, E. N.; Glass, H. F.; Liu, Z.; Bayley, P. M.; Dutton, S. E.; Grey, C. P.; Wright, D. S. $Mg(PF_6)_2$-Based Electrolyte Systems: Understanding Electrolyte-Electrode Interactions for the Development of Mg-Ion Batteries. *J. Am. Chem. Soc.* **2016**, *138,* 8682-8685.

(11)   Ha, S. Y.; Lee, Y. W.; Woo, S. W.; Koo, B.; Kim, J. S.; Cho, J.; Lee, K. T.; Choi, N. S. Magnesium(Ii) Bis(Trifluoromethane Sulfonyl) Imide-Based Electrolytes with Wide Electrochemical Windows for Rechargeable Magnesium Batteries. *ACS Appl. Mater. Interfaces* **2014**, *6,* 4063-4073.

(12)   Mohtadi, R.; Matsui, M.; Arthur, T. S.; Hwang, S. J. Magnesium Borohydride: From Hydrogen Storage to Magnesium Battery. *Angew. Chem. Int. Ed.* **2012**, *51,* 9780-9783.

(13)   Shao, Y. Y.; Liu, T. B.; Li, G. S.; Gu, M.; Nie, Z. M.; Engelhard, M.; Xiao, J.; Lv, D. P.; Wang, C. M.; Zhang, J. G.; Liu, J. Coordination Chemistry in Magnesium Battery Electrolytes: How Ligands Affect their Performance. *Sci. Rep.* **2013**, *3*, 3130.

(14)   Aurbach, D.; Gizbar, H.; Schechter, A.; Chusid, O.; Gottlieb, H. E.; Gofer, Y.; Goldberg, I. Electrolyte Solutions for Rechargeable Magnesium Batteries Based on Organomagnesium Chloroaluminate Complexes. *J. Electrochem. Soc.* **2002**, *149,* A115-A121.

(15)   Pour, N.; Gofer, Y.; Major, D. T.; Aurbach, D. Structural Analysis of Electrolyte
        Solutions for Rechargeable Mg Batteries by Stereoscopic Means and Dft Calculations.
        J. Am. Chem. Soc. **2011**, *133,* 6270-6278.

(16)   Bucur, C. B.; Gregory, T.; Oliver, A. G.; Muldoon, J. Confession of a Magnesium
        Battery. *J. Phys. Chem. Lett.* **2015**, *6,* 3578-3591.

(17)   Muldoon, J.; Bucur, C. B.; Oliver, A. G.; Zajicek, J.; Allred, G. D.; Boggess, W. C.
        Corrosion of Magnesium Electrolytes: Chlorides - the Culprit. *Energy Environ. Sci.*
        2013, *6,* 482-487.

(18)   Wu, N.; Yang, Z. Z.; Yao, H. R.; Yin, Y. X.; Gu, L.; Guo, Y. G. Improving the
        Electrochemical Performance of the $Li_4Ti_5O_{12}$ Electrode in a Rechargeable Magnesium
        Battery by Lithium-Magnesium Co-Intercalation. *Angew. Chem. Int. Ed.* **2015**, *54,* 5757-
        5761.

(19)   Cheng, Y.; Liu, T.; Shao, Y.; Engelhard, M. H.; Liu, J.; Li, G. Electrochemically Stable
        Cathode Current Collectors for Rechargeable Magnesium Batteries. *J. Mater. Chem. A*
        2014, *2,* 2473-2477.

(20)   Arthur, T. S.; Zhang, R.; Ling, C.; Glans, P. A.; Fan, X.; Guo, J.; Mizuno, F.
        Understanding the Electrochemical Mechanism of K-αMnO_2 for Magnesium Battery
        Cathodes. *ACS Appl. Mater. Interfaces* **2014**, *6,* 7004-7008.

(21)   Xie, J.; Li, C.; Cui, Z.; Guo, X. Transition-Metal-Free Magnesium-Based Batteries
        Activated by Anionic Insertion into Fluorinated Graphene Nanosheets. *Adv. Funct.*
        Mater. **2015**, *25,* 6519-6526.

(22)   Zhang, Y.; Xie, J.; Han, Y.; Li, C. Dual-Salt Mg-Based Batteries with Conversion Cathodes. *Adv. Funct. Mater.* **2015**, *25,* 7300-7308.

(23)   Cheng, Y.; Shao, Y.; Raju, V.; Ji, X.; Mehdi, B. L.; Han, K. S.; Engelhard, M. H.; Li, G.; Browning, N. D.; Mueller, K. T.; Liu, J. Molecular Storage of Mg Ions with Vanadium Oxide Nanoclusters. *Adv. Funct. Mater.* **2016**, *26,* 3446-3453.

(24)   Pan, B.; Huang, J.; Feng, Z.; Zeng, L.; He, M.; Zhang, L.; Vaughey, J. T.; Bedzyk, M. J.; Fenter, P.; Zhang, Z.; Burrell, A. K.; Liao, C. Polyanthraquinone-Based Organic Cathode for High-Performance Rechargeable Magnesium-Ion Batteries. *Adv. Energy Mater.* **2016**, *6,* 1600140.

(25)   Wang, L.; Asheim, K.; Vullum, P. E.; Svensson, A. M.; Vullum-Bruer, F. Sponge-Like Porous Manganese(II,III) Oxide as a Highly Efficient Cathode Material for Rechargeable Magnesium Ion Batteries. *Chem. Mater.* **2016**, *28,* 6459-6470.

(26)   Aurbach, D.; Lu, Z.; Schechter, A.; Gofer, Y.; Gizbar, H.; Turgeman, R.; Cohen, Y.; Moshkovich, M.; Levi, E. Prototype Systems for Rechargeable Magnesium Batteries. *Nature* **2000**, *407,* 724-727.

(27)   Lancry, E.; Levi, E.; Gofer, Y.; Levi, M.; Salitra, G.; Aurbach, D. Leaching Chemistry and the Performance of the Mo_6S_8 Cathodes in Rechargeable Mg Batteries. *Chem. Mater.* **2004**, *16,* 2832-2838.

(28)   Novak, P.; Scheifele, W.; Haas, O. Magnesium Insertion Batteries - an Alternative to Lithium. *J. Power Sources* **1995**, *54,* 479-482.

(29)   Spahr, M. E.; Novak, P.; Haas, O.; Nesper, R. Electrochemical Insertion of Lithium, Sodium, and Magnesium in Molybdenum(VI) Oxide. *J. Power Sources* **1995**, *54,* 346-351.

(30)   Gershinsky, G.; Yoo, H. D.; Gofer, Y.; Aurbach, D. Electrochemical and Spectroscopic Analysis of Mg^{2+} Intercalation into Thin Film Electrodes of Layered Oxides: V_2O_5 and MoO_3. *Langmuir* **2013**, *29,* 10964-10972.

(31)   Liang, Y. L.; Feng, R. J.; Yang, S. Q.; Ma, H.; Liang, J.; Chen, J. Rechargeable Mg Batteries with Graphene-Like MoS_2 Cathode and Ultrasmall Mg Nanoparticle Anode. *Adv. Mater.* **2011**, *23,* 640-643.

(32)   Liu, Y. C.; Jiao, L. F.; Wu, Q.; Du, J.; Zhao, Y. P.; Si, Y. C.; Wang, Y. J.; Yuan, H. T. Sandwich-Structured Graphene-Like MoS_2/C Microspheres for Rechargeable Mg Batteries. *J. Mater. Chem. A* **2013**, *1,* 5822-5826.

(33)   Sun, X.; Bonnick, P.; Duffort, V.; Liu, M.; Rong, Z.; Persson, K. A.; Ceder, G.; Nazar, L. F. A High Capacity Thiospinel Cathode for Mg Batteries. *Energy Environ. Sci.* **2016**, *9,* 2273-2277.

(34)   Wan, L. W. F.; Perdue, B. R.; Apblett, C. A.; Prendergast, D. Mg Desolvation and Intercalation Mechanism at the Mo_6S_8 Chevrel Phase Surface. *Chem. Mater.* **2015**, *27,* 5932-5940.

(35)   Mizuno, F.; Singh, N.; Arthur, T. S.; Fanson, P. T.; Ramanathan, M.; Benmayza, A.; Prakash, J.; Liu, Y. S.; Glans, P. A.; Guo, J. Understanding and Overcoming the

Challenges Posed by Electrode/Electrolyte Interfaces in Rechargeable Magnesium Batteries. *Front. Energy Res.* **2014**, *2*.

(36)   Tian, H.; Gao, T.; Li, X.; Wang, X.; Luo, C.; Fan, X.; Yang, C.; Suo, L.; Ma, Z.; Han, W.; Wang, C. High Power Rechargeable Magnesium/Iodine Battery Chemistry. *Nat. Commun.* **2017**, *8,* 14083.

(37)   Mizrahi, O.; Amir, N.; Pollak, E.; Chusid, O.; Marks, V.; Gottlieb, H.; Larush, L.; Zinigrad, E.; Aurbach, D. Electrolyte Solutions with a Wide Electrochemical Window for Recharge Magnesium Batteries. *J. Electrochem. Soc.* **2008**, *155,* A103-A109.

(38)   Augustyn, V.; Simon, P.; Dunn, B. Pseudocapacitive Oxide Materials for High-Rate Electrochemical Energy Storage. *Energy Environ. Sci.* **2014**, *7,* 1597-1614.

(39)   Wang, J.; Polleux, J.; Lim, J.; Dunn, B. Pseudocapacitive Contributions to Electrochemical Energy Storage in TiO_2 (Anatase) Nanoparticles. *J. Phys. Chem. C* **2007**, *111,* 14925-14931.

(40)   Augustyn, V.; Come, J.; Lowe, M. A.; Kim, J. W.; Taberna, P. L.; Tolbert, S. H.; Abruna, H. D.; Simon, P.; Dunn, B. High-Rate Electrochemical Energy Storage through Li^+ Intercalation Pseudocapacitance. *Nat. Mater.* **2013**, *12,* 518-522.

(41)   Chao, D.; Zhu, C.; Yang, P.; Xia, X.; Liu, J.; Wang, J.; Fan, X.; Savilov, S. V.; Lin, J.; Fan, H. J.; Shen, Z. X. Array of Nanosheets Render Ultrafast and High-Capacity Na-Ion Storage by Tunable Pseudocapacitance. *Nat. Commun.* **2016**, *7,* 12122.

(42)   Zhang, R.; Yu, X.; Nam, K. W.; Ling, C.; Arthur, T. S.; Song, W.; Knapp, A. M.; Ehrlich, S. N.; Yang, X. Q.; Matsui, M. α-MnO₂ as a Cathode Material for Rechargeable Mg Batteries. *Electrochem. Commun.* **2012**, *23,* 110-113.

(43)   Stankovich, S.; Dikin, D. A.; Piner, R. D.; Kohlhaas, K. A.; Kleinhammes, A.; Jia, Y.; Wu, Y.; Nguyen, S. T.; Ruoff, R. S. Synthesis of Graphene-Based Nanosheets *Via* Chemical Reduction of Exfoliated Graphite Oxide. *Carbon* **2007**, *45,* 1558-1565.

(44)   Hummers, W. S.; Offeman, R. E. Preparation of Graphitic Oxide. *J. Am. Chem. Soc.* **1958**, *80,* 1339-1339.

(45)   Song, L.; Ci, L.; Lu, H.; Sorokin, P. B.; Jin, C.; Ni, J.; Kvashnin, A. G.; Kvashnin, D. G.; Lou, J.; Yakobson, B. I.; Ajayan, P. M. Large Scale Growth and Characterization of Atomic Hexagonal Boron Nitride Layers. *Nano Lett.* **2010**, *10,* 3209-3215.

(46)   God, C.; Bitschnau, B.; Kapper, K.; Lenardt, C.; Schmuck, M.; Mautner, F.; Koller, S. Intercalation Behaviour of Magnesium into Natural Graphite Using Organic Electrolyte Systems. *RSC Adv.* **2017**, *7,* 14168-14175.

(47)   Kumar, N.; Siegel, D. J. Interface-Induced Renormalization of Electrolyte Energy Levels in Magnesium Batteries. *J. Phys. Chem. Lett.* **2016**, *7,* 874-881.

(48)   Er, D.; Detsi, E.; Kumar, H.; Shenoy, V. B. Defective Graphene and Graphene Allotropes as High-Capacity Anode Materials for Mg Ion Batteries. *ACS Energy Lett.* **2016**, *1,* 638-645.

(49)   Gauthier, M.; Carney, T. J.; Grimaud, A.; Giordano, L.; Pour, N.; Chang, H.; Fenning, D. P.; Lux, S. F.; Paschos, O.; Bauer, C.; Maglia, F.; Lupart, S.; Lamp, P.; Horn, Y. S.

Electrode-Electrolyte Interface in Li-Ion Batteries: Current Understanding and New Insights. *J. Phys. Chem. Lett.* **2015**, *6*, 4653-4672.

(50)   Liu, H.; Wang, J.; Zhang, X.; Zhou, D.; Qi, X.; Qiu, B.; Fang, J.; Kloepsch, R.; Schumacher, G.; Liu, Z.; Li, J. Morphological Evolution of High-Voltage Spinel $LiNi_{0.5}Mn_{1.5}O_4$ Cathode Materials for Lithium-Ion Batteries: The Critical Effects of Surface Orientations and Particle Size. *ACS Appl. Mater. Interfaces* **2016**, *8*, 4661-4675.

(51)   Ma, J.; Hu, P.; Cui, G.; Chen, L. Surface and Interface Issues in Spinel $LiNi_{0.5}Mn_{1.5}O_4$: Insights into a Potential Cathode Material for High Energy Density Lithium Ion Batteries. *Chem. Mater.* **2016**, *28*, 3578-3606.

(52)   Nguyen, D. T.; Tran, X. M.; Kang, J.; Song, S. W. Magnesium Storage Performance and Surface Film Formation Behavior of Tin Anode Material. *ChemElectroChem* **2016**, *3,* 1813-1819.

(53)   Barile, C. J.; Spatney, R.; Zavadil, K. R.; Gewirth, A. A. Investigating the Reversibility of *in Situ* Generated Magnesium Organohaloalurninates for Magnesium Deposition and Dissolution. *J. Phys. Chem. C* **2014**, *118,* 10694-10699.

(54)   Barile, C. J.; Barile, E. C.; Zavadil, K. R.; Nuzzo, R. G.; Gewirth, A. A. Electrolytic Conditioning of a Magnesium Aluminum Chloride Complex for Reversible Magnesium Deposition. *J. Phys. Chem. C* **2014**, *118,* 27623-27630.

(55)   Metsger, L.; Bittner, S. Autocatalytic Oxidation of Ethers with Sodium Bromate. *Tetrahedron* **2000**, *56,* 1905-1910.

(56)   Wang, T. J.; Ma, Z. H.; Huang, M. Y.; Jiang, Y. Y. Selective Oxidation of Tetrahydrofuran with Molecular Oxygen Catalyzed by Polyalumazane-Platinum Complexes. *Poly. Adv. Technol.* **1996**, *7,* 88-91.

(57)   Sommovigo, M.; Alper, H. Aerobic Oxidation of Ethers and Alkenes Catalyzed by a Novel Palladium Complex. *J. Mol. Catal.* **1994**, *88,* 151-158.

(58)   Fazlurrahman, A. K.; Tsai, J. C.; Nicholas, K. M. Rhodium-Catalyzed, Carbon Dioxide-Mediated Aerobic Oxidation of Ethers. *J. Chem. Soc. Chem. Comm.* **1992**, 1334-1335.

(59)   Avgousti, C.; Georgolios, N.; Kyriacou, G.; Ritzoulis, G. The Electrochemical Oxidation of Tetrahydrofuran in Sulphuric Acid Solution. *Electrochim. Acta* **1999**, *44,* 3295-3301.

(60)   Lindstrom, H.; Sodergren, S.; Solbrand, A.; Rensmo, H.; Hjelm, J.; Hagfeldt, A.; Lindquist, S. E. Li^+ Ion Insertion in TiO_2 (Anatase). 2. Voltammetry on Nanoporous Films. *J. Phys. Chem. B* **1997**, *101,* 7717-7722.

(61)   Conway, B. E.; Birss, V.; Wojtowicz, J. The Role and Utilization of Pseudocapacitance for Energy Storage by Supercapacitors. *J. Power Sources* **1997**, *66,* 1-14.

(62)   Benmayza, A.; Ramanathan, M.; Arthur, T. S.; Matsui, M.; Mizuno, F.; Guo, J.; Glans, P. A.; Prakash, J. Effect of Electrolytic Properties of a Magnesium Organohaloaluminate Electrolyte on Magnesium Deposition. *J. Phys. Chem. C* **2013**, *117,* 26881-26888.

(63)   Canepa, P.; Gautam, G. S.; Malik, R.; Jayaraman, S.; Rong, Z.; Zavadil, K. R.; Persson, K.; Ceder, G. Understanding the Initial Stages of Reversible Mg Deposition and Stripping in Inorganic Nonaqueous Electrolytes. *Chem. Mater.* **2015**, *27,* 3317-3325.

(64)   Ling, C.; Zhang, R. G.; Arthur, T. S.; Mizuno, F. How General is the Conversion Reaction in Mg Battery Cathode: A Case Study of the Magnesiation of α-MnO_2. *Chem. Mater.* **2015**, *27,* 5799-5807.

(65)   Wang, L.; Wang, Z.; Vullum, P. E.; Selbach, S. M.; Svensson, A. M.; Vullum-Bruer, F. Solvent-Controlled Charge Storage Mechanisms of Spinel Oxide Electrodes in Mg Organohaloaluminate Electrolytes. *Nano Lett.* **2018**, *18*, 763-772.

(66)   Kim, J. S.; Chang, W. S.; Kim, R. H.; Kim, D. Y.; Han, D. W.; Lee, K. H.; Lee, S. S.; Doo, S. G. High-Capacity Nanostructured Manganese Dioxide Cathode for Rechargeable Magnesium Ion Batteries. *J. Power Sources* **2015**, *273,* 210-215.

(67)   An, Q.; Li, Y.; Deog Yoo, H.; Chen, S.; Ru, Q.; Mai, L.; Yao, Y. Graphene Decorated Vanadium Oxide Nanowire Aerogel for Long-Cycle-Life Magnesium Battery Cathodes. *Nano Energy* **2015**, *18,* 265-272.

(68)   Inamoto, M.; Kurihara, H.; Yajima, T. Vanadium Pentoxide-Based Composite Synthesized Using Microwave Water Plasma for Cathode Material in Rechargeable Magnesium Batteries. *Materials* **2013**, *6,* 4514-4522.

(69)   Orikasa, Y.; Masese, T.; Koyama, Y.; Mori, T.; Hattori, M.; Yamamoto, K.; Okado, T.; Huang, Z. D.; Minato, T.; Tassel, C.; Kim, J.; Kobayashi, Y.; Abe, T.; Kageyama, H.; Uchimoto, Y. High Energy Density Rechargeable Magnesium Battery Using Earth-Abundant and Non-Toxic Elements. *Sci. Rep.* **2014**, *4,* 5622.

(70)   Tao, Z. L.; Xu, L. N.; Gou, X. L.; Chen, J.; Yuan, H. T. TiS_2 Nanotubes as the Cathode Materials of Mg-Ion Batteries. *Chem. Commun.* **2004**, 2080-2081.

(71)   Liu, B.; Luo, T.; Mu, G. Y.; Wang, X. F.; Chen, D.; Shen, G. Z. Rechargeable Mg-Ion Batteries Based on WSe$_2$ Nanowire Cathodes. *ACS Nano* **2013**, *7,* 8051-8058.

(72)   Tashiro, Y.; Taniguchi, K.; Miyasaka, H. Copper Selenide as a New Cathode Material Based on Displacement Reaction for Rechargeable Magnesium Batteries. *Electrochim. Acta* **2016**, *210,* 655-661.

(73)   Zhang, R.; Mizuno, F.; Ling, C. Fullerenes: Non-Transition Metal Clusters as Rechargeable Magnesium Battery Cathodes. *Chem. Commun.* **2015**, *51,* 1108-1111.

(74)   Pan, B.; Zhou, D.; Huang, J.; Zhang, L.; Burrell, A. K.; Vaughey, J. T.; Zhang, Z.; Liao, C. 2,5-Dimethoxy-1,4-Benzoquinone (DMBQ) as Organic Cathode for Rechargeable Magnesium-Ion Batteries. *J. Electrochem. Soc.* **2016**, *163,* A580-A583.

(75)   Bitenc, J.; Pirnat, K.; Bancic, T.; Gaberscek, M.; Genorio, B.; Randon, V. A.; Dominko, R. Anthraquinone-Based Polymer as Cathode in Rechargeable Magnesium Batteries. *Chemsuschem* **2015**, *8,* 4128-4132.

(76)   Montes, J. M.; Cuevas, F. G.; Cintas, J.; Urban, P. Electrical Conductivity of Metal Powders under Pressure. *Appl. Phys. A* **2011**, *105,* 935-947.

(77)   Kresse, G.; Furthmuller, J. Efficient Iterative Schemes for ab Initio Total-Energy Calculations Using a Plane-Wave Basis Set. *Phys. Rev. B* **1996**, *54,* 11169-11186.

(78)   Kresse, G.; Joubert, D. From Ultrasoft Pseudopotentials to the Projector Augmented-Wave Method. *Phys. Rev. B* **1999**, *59,* 1758-1775.

(79)   Perdew, J. P.; Ruzsinszky, A.; Csonka, G. I.; Vydrov, O. A.; Scuseria, G. E.; Constantin, L. A.; Zhou, X. L.; Burke, K. Restoring the Density-Gradient Expansion for Exchange in Solids and Surfaces. *Phys. Rev. Lett.* **2008**, *100*, 136406.

(80)   Perdew, J. P.; Burke, K.; Ernzerhof, M. Generalized Gradient Approximation Made Simple. *Phys. Rev. Lett.* **1996**, *77*, 3865-3868.

(81)   Mathew, K.; Sundararaman, R.; Letchworth, W. K.; Arias, T. A.; Hennig, R. G. Implicit Solvation Model for Density-Functional Study of Nanocrystal Surfaces and Reaction Pathways. *J. Chem. Phys.* **2014**, *140*, 084106.

(82)   Fishman, M.; Zhuang, H. L. L.; Mathew, K.; Dirschka, W.; Hennig, R. G. Accuracy of Exchange-Correlation Functionals and Effect of Solvation on the Surface Energy of Copper. *Phys. Rev. B* **2013**, *87*, 245402.

Table of content

$[Mg_2(\mu\text{-}Cl)_3\cdot 6THF]^+$

$[Mg_2(\mu\text{-}Cl)_3\cdot 6DME]^+$